

κ monty: a Monte Carlo Compton Scattering code including non-thermal electrons

Jordy Davelaar^{1,2*}, Benjamin R. Ryan³, George N. Wong^{4,5}, Thomas Bronzwaer⁶, Hector Olivares⁶, Monika Mościbrodzka⁶, Charles F. Gammie^{7,8}, and Heino Falcke⁶

¹*Department of Astronomy and Columbia Astrophysics Laboratory, Columbia University, 550 W 120th St, New York, NY 10027, USA*

²*Center for Computational Astrophysics, Flatiron Institute, 162 Fifth Avenue, New York, NY 10010, USA*

³*CCS-2, Los Alamos National Laboratory, P.O. Box 1663, Los Alamos, NM 87545, US*

⁴*School of Natural Sciences, Institute for Advanced Study, 1 Einstein Drive, Princeton, NJ 08540, USA*

⁵*Princeton Gravity Initiative, Princeton University, Princeton, New Jersey 08544, USA*

⁶*Department of Astrophysics/IMAPP, Radboud University, P.O. Box 9010, 6500 GL, Nijmegen, The Netherlands*

⁷*Illinois Center for Advanced Studies of the Universe, Department of Physics, University of Illinois, 1110 West Green St, Urbana, IL 61801, USA*

⁸*Department of Astronomy, University of Illinois, 1002 West Green Street, Urbana, IL 61801, USA*

Accepted 2023 September 29. Received 2023 September 29; in original form 2023 March 24

ABSTRACT

Low-luminosity active galactic nuclei are strong sources of X-ray emission produced by Compton scattering originating from the accretion flows surrounding their supermassive black holes. The shape and energy of the resulting spectrum depend on the shape of the underlying electron distribution function (DF). In this work, we present an extended version of the `grmonty` code, called `κ monty`. The `grmonty` code previously only included a thermal Maxwell Jüttner electron distribution function. We extend the `grmonty` code with non-thermal electron DFs, namely the κ and power-law DFs, implement Cartesian Kerr-Schild coordinates, accelerate the code with MPI, and couple the code to the non-uniform AMR grid data from the GRMHD code `BHAC`. For the Compton scattering process, we derive two sampling kernels for both distribution functions. Finally, we present a series of code tests to verify the accuracy of our schemes. The implementation of non-thermal DFs opens the possibility of studying the effect of non-thermal emission on previously developed black hole accretion models.

Key words: plasmas – radiative transfer – radiation mechanisms: non-thermal – software: development – software: public release

1 INTRODUCTION

Active Galactic Nuclei (AGN) are strong sources of radiation over the full range of the electromagnetic spectrum, from radio up to γ -rays. The emission is expected to originate from a relativistic plasma flow close to these galaxies' central supermassive black holes. Low-luminosity AGN (LLAGN) are well-known sources of X-ray emission. Sagittarius A* (SgrA*), the black hole in the centre of the milky way, shows X-ray variability on the time scales of hours (Baganoff et al. 2003; Eckart et al. 2004). Messier 87 (M87), now famous for the first picture of a black hole shadow by the event horizon telescope collaboration (EHT) (EHT Collaboration et al. 2019a), is also active in X-ray emissions (Wilson and Yang 2001; Marshall et al. 2002; Perlman and Wilson 2005; Prieto et al. 2016), and shows X-ray variability on timescales

of days (Harris et al. 2009). One channel to generate the X-ray emission is via inverse Compton (IC) scattering.

To compute synthetic spectra of LLAGN, a variety of Monte Carlo codes have been developed (see e.g. Yao et al. (2005); Stern et al. (1995); Schnittman et al. (2006); Schnittman and Krolik (2009); Laurent and Titarchuk (1999); Böttcher and Liang (2001); Böttcher et al. (2003); Dolence et al. (2009); Ryan et al. (2015); Narayan et al. (2016); Zhang et al. (2019); Mościbrodzka (2020)). A large subset of the code uses the input from general relativistic magnetohydrodynamics (GRMHD) global simulations of weakly radiating accretion flows. In these simulations, the electron energy distribution function is not explicitly computed. GRMHD codes use a fluid approximation that only contains information on the bulk properties of the plasma and no information on the distribution function. A fluid approach also does not intrinsically contain collisionless effects. However, accretion flows in LLAGN like M87* and SgrA* have a mean free path for the electrons that is much large

* E-mail: j.davelaar@columbia.edu

than the actual system size, making them effectively collisionless, and deviations from thermality are, therefore, to be expected. Magnetic reconnection, dissipation of turbulent energy, shocks, and/or other plasma instabilities that influence the shape of the electron distribution function are, in general, poorly resolved, and sub-grid models for electron heating and acceleration have to be invoked. Successful attempts to resolve magnetic reconnection in global two-dimensional GRMHD simulation have been performed by Ripperda et al. (2020); Nathanael et al. (2020) and, more recently, in three-dimensional simulations by Ripperda et al. (2022). These models further strengthen the need for non-thermal electron distribution functions.

One of the first attempts to model non-thermal emission from SgrA* with radiatively inefficient accretion flows (RIAF) models were made by Özel et al. (2000). Later works using RIAF models include Yuan et al. (2003), among others. Semi-analytical models of RIAFs, including jets, were developed by Broderick et al. (2015), who included electron acceleration via gap acceleration. Works by (Quataert 2004; Chan et al. 2015b,a) showed that for Sgr A* that X-ray bremsstrahlung emission is non-negligible. More recently, dynamical models based on GRMHD simulations were published by Chan et al. (2009); Ball et al. (2016); Mao et al. (2017); Chael et al. (2017); Davelaar et al. (2018b, 2019); Chatterjee et al. (2020); Cruz-Osorio et al. (2022); Fromm et al. (2022). A common conclusion in all these works is that non-thermal electrons enhance the amount of NIR and radio emission. However, most of these works rely on General Relativistic Ray Tracing methods, so X-ray emission generated via IC is neither included nor approximated.

The importance of including X-ray emission in the current models used within the EHT community was shown by Mościbrodzka et al. (2016). For M87, the X-ray emission is a clear discriminator between models. If the electron temperature in the accretion disk is too high, the model easily overproduces the observed X-ray flux. However, the electron distribution function was assumed to be a thermal Maxwell-Jüttner distribution.

The X-ray emission is expected to be produced by Synchrotron Self Comptonisation. This process starts with electrons in the accretion flow that gyrate around magnetic field lines and produce emission via synchrotron emission. The emitted photons are then upscattered by the hot relativistic electrons inside the flow to X-ray and γ -ray energies via Compton scattering. Since the amount of energy that is transferred from the electron to the photon (ΔE) depends on the Lorentz factor of the electron (γ) as $\Delta E \propto \gamma^2$, the resulting spectra of the upscattered photons depend on the choice of the distribution function. It is expected that adding accelerated particles will increase the total X-ray luminosity of the source since electrons with large γ factors and photons with larger frequencies (NIR) are present. Observed X-ray flares in AGN, and other astrophysical sources, are indicators of ongoing particle acceleration to rule out potential acceleration mechanisms models that include the generation of X-ray emission based on non-thermal electrons are needed.

In this work, we present κ monty¹ a new flavour of the Monte Carlo code `grmonty` originally developed by Dolence

et al. (2012). `grmonty` is a general relativistic Monte Carlo radiative transport code developed to compute spectra of accreting black holes. A more recent version called RADPOL (Mościbrodzka 2020) also included polarisation and was extended to include non-thermal electron distribution functions (Mościbrodzka 2022). We made three large adaptations to the original Dolence et al. (2012) code. First, we coupled our code to the non-uniform adaptive mesh refinement (AMR) grid data structure of the GRMHD code BHAC (Porth et al. 2017; Olivares et al. 2019, www.bhac.science), in a similar manner as we described in Davelaar et al. (2019). Second, we implemented the fit formula for the emission and absorption coefficients as obtained by Pandya et al. (2016) for the initial seed photons. Third, we derived and implemented semi-analytical sampling algorithms for the κ and power-law distribution function. The methods described in this work were used to compute the X-ray SEDs of the κ -DF based models in the Event Horizon Telescope results of Sagittarius A* (Event Horizon Telescope Collaboration 2022).

In Section 2, we explain our sampling routine and describe the setup used. In Section 3, we perform a variety of code tests. We discuss and summarise our results in Section 5.

2 METHODS

In this section, we present the additions we made to the original `grmonty` code (Dolence et al. 2009). Our new code κ monty includes the κ distribution and power-law distribution to study accelerated particle emission and is `mpi` and `openmp` optimised. At first, the superphotons, a packet of photons with weight w , where the weight is w is the number of real photons represented by the superphoton, are initialised by either thermal, κ , or power-law-based emission coefficients. As they propagate through the plasma, the total intensity decreases due to absorption. Scattering events are selected based on the mean free path length. If a photon is selected for scattering, the electron has to be drawn from the relevant distribution function. In this section, we summarise the new features of κ monty, which are new sets of coordinates, new distribution functions, and the coupling to non-uniform data formats. For a complete explanation of the initialisation, integration, and scattering of the superphotons, see the paper by Dolence et al. (2009). In this section, we will give a global summary of the different aspects of the code, and we will explain in detail our modifications.

2.1 Geodesic integration

The trajectory of the superphotons is computed by solving the geodesic equation,

$$\frac{d^2 x^\alpha}{d\lambda^2} = -\Gamma_{\mu\nu}^\alpha \frac{dx^\mu}{d\lambda} \frac{dx^\nu}{d\lambda}, \quad (1)$$

where $\Gamma_{\mu\nu}^\alpha$ are the Christoffel symbols, and λ the affine parameter. The Christoffel symbols depend on derivatives of the metric and are given by,

$$\Gamma_{\mu\nu}^\alpha = \frac{1}{2} g^{\alpha\rho} [\partial_\mu g_{\nu\rho} + \partial_\nu g_{\mu\rho} - \partial_\rho g_{\mu\nu}]. \quad (2)$$

¹ Publicly available at: <https://github.com/jordydavelaar/kmonty>

The Christoffel symbols are either provided analytically or can be computed by computing the metric derivatives using a second-order finite difference method.

2.1.1 Kerr-Schild coordinates

A rotating black hole is described by the Kerr metric (Kerr 1963). In spherical Kerr-Schild horizon penetrating coordinates the non-zero covariant components of the metric² $g_{\mu\nu}$ are given by

$$g_{tt} = - \left(1 - \frac{2r}{\Sigma} \right) \quad (3a)$$

$$g_{t\phi} = g_{\phi t} = - \frac{2ra_* \sin^2 \theta}{\Sigma} \quad (3b)$$

$$g_{rr} = \frac{\Sigma}{\Delta} \quad (3c)$$

$$g_{\theta\theta} = \Sigma \quad (3d)$$

$$g_{\phi\phi} = \left(r^2 + a_*^2 + \frac{2ra_*^2}{\Sigma} \sin^2 \theta \right) \sin^2 \theta \quad (3e)$$

for a black hole with unitary mass $M = 1$ and angular momentum J , where $a_* = J/(Mc)$ is the dimensionless spin parameter, $\Sigma = r^2 + a_*^2 \cos^2 \theta$, and $\Delta = r^2 - 2r + a_*^2$.

The GRMHD code used in this work BHAC primarily uses for the EHT GRMHD library (EHT Collaboration et al. 2019b) Modified Kerr-Schild coordinates where the r and θ coordinates are modified. The coordinates (t, X_1, X_2, X_3) are related to standard KS via

$$t = t \quad (4a)$$

$$r = \exp(X_1) \quad (4b)$$

$$\theta = X_2 + \frac{h}{2} \sin(2X_2) \quad (4c)$$

$$\phi = X_3 \quad (4d)$$

This results in a grid that is logarithmic spaced in radius and concentrated towards the midplane in θ , set by the h parameter. Transforming the metric to MKS is done via multiplication of the metric terms with the non-zero elements of the Jacobian,

$$\partial r / \partial x_1 = r \quad (5a)$$

$$\partial \theta / \partial X_2 = 1 + h \cos(2X_2). \quad (5b)$$

2.1.2 Cartesian Kerr-Schild coordinates

We extended the code to include Cartesian Kerr-Schild (CKS) coordinates, which relate to spherical Kerr-Schild coordinates via

$$t = t \quad (6a)$$

$$x = r(\cos(\hat{\phi}) + a_* \sin(\hat{\phi})) \sin(\theta) \quad (6b)$$

$$y = r(\sin(\hat{\phi}) - a_* \cos(\hat{\phi})) \sin(\theta) \quad (6c)$$

$$z = r \cos(\theta). \quad (6d)$$

² We use the metric signature $(-, +, +, +)$.

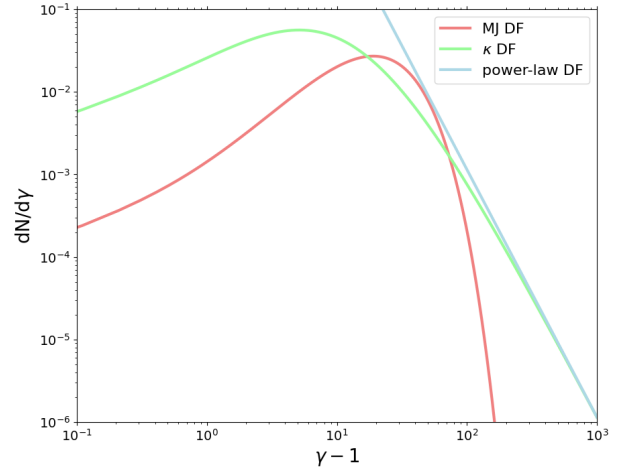


Figure 1. The Maxwell-Jüttner (MJ), κ and power-law distribution functions (DF). The MJ DF is shown for a dimensionless electron temperature of $\Theta_e = 10$, the κ DF is shown with $\kappa = 4.0$, and $w = 2.5$, and the power-law DF is shown with $p = 3$, $\gamma_{\min} = 25$, and $\gamma_{\max} = 10^3$.

The covariant Cartesian KS metric, $g_{\mu\nu}$, is given by (Kerr 1963)

$$g_{\mu\nu} = \eta_{\mu\nu} + fl_{\mu}l_{\nu}, \quad (7)$$

here $\eta_{\mu\nu}$ is the Minkowski metric and is given by $\eta_{\mu\nu} = \text{diag}(-1, 1, 1, 1)$, and

$$f = \frac{2r^3}{r^4 + a_*^2 z^2}, \quad (8a)$$

$$l_{\nu} = \left(1, \frac{rx + a_*y}{r^2 + a_*^2}, \frac{ry - a_*x}{r^2 + a_*^2}, \frac{z}{r} \right), \quad (8b)$$

where r is given by

$$r^2 = \frac{R^2 - a_*^2 + \sqrt{(R^2 - a_*^2)^2 + 4a_*^2 z^2}}{2}, \quad (9)$$

and

$$R^2 = x^2 + y^2 + z^2. \quad (10)$$

In the limit of $R \gg a_*$, the radius $r \rightarrow R$. The contravariant metric is defined as

$$g^{\mu\nu} = \eta^{\mu\nu} - fl^{\mu}l^{\nu}, \quad (11)$$

where l^{ν} is given by

$$l^{\nu} = \left(-1, \frac{rx + a_*y}{r^2 + a_*^2}, \frac{ry - a_*x}{r^2 + a_*^2}, \frac{z}{r} \right). \quad (12)$$

2.2 Distribution functions

For the distribution function, we either use a Maxwell-Jüttner (MJ) distribution function (DF), a κ -DF, or a power-law-DF. All three distribution functions are isotropic.

The MJ DF is given by

$$\frac{dn_e}{d\gamma} = \frac{n_e}{\Theta_e K_2(\Theta_e^{-1})} \exp\left(-\frac{\gamma}{\Theta_e}\right), \quad (13)$$

where γ_e is the Lorentz factor of the electrons, n_e the number density of electrons, Θ_e the dimensionless electron temperature, and K_2 the modified Bessel function of the second kind. For the thermal DF, the emission coefficients used in `κmonty` can be found in [Leung et al. \(2011a\)](#).

The κ DF is used to describe the particle population of a variety of space plasma, such as the solar wind ([Decker and Krimigis 2003](#)), coronal flares on the Sun ([Livadiotis and McComas 2013](#)), turbulent flows ([Kunz et al. 2016](#)), and jets ([Davelaar et al. 2018b](#)). X-ray spectra generated based on this distribution function could, therefore, be of interest to a broad range of astrophysical problems. The DF in relativistic form ([Xiao 2006](#)) is given by,

$$\frac{dn_e}{d\gamma} = n_e N \gamma \sqrt{\gamma^2 - 1} \left(1 + \frac{\gamma - 1}{\kappa w}\right)^{-(\kappa+1)}, \quad (14)$$

where the κ -parameter sets the power law-index via $\kappa = p + 1$, w is the width of the distribution function, and N is a normalisation constant. In the κ case, the normalisation constant N is not known analytically and is, therefore, when needed, computed during run time with a `gsl` integrator by demanding that

$$\int_1^\infty \frac{dn_e}{n_e d\gamma} d\gamma = 1. \quad (15)$$

The emission coefficients for the κ -DF can be found in [Pandya et al. \(2016\)](#).

Finally, the power-law DF is given by

$$\frac{dn_e}{d\gamma} = n_e \frac{(p-1)\gamma^{-p}}{(\gamma_{\min}^{1-p} - \gamma_{\max}^{1-p})}, \quad (16)$$

where p is the power-law index. The DF function is non-zero only when γ is between γ_{\min} and γ_{\max} . The emission coefficients for the power law-DF can be found in [Pandya et al. \(2016\)](#).

All three DFs are shown in figure 1. The dependence of the DF in the code can be found in three places; the emission coefficients, the cross-section for scattering, and the sampling of the DF if a scattering event takes place. In the remainder of this section, we will explain what changes we made to the code for each of these.

2.3 Emission coefficients

For the emission coefficients, the code uses fit formulas from [Leung et al. \(2011b\)](#) for the thermal distribution function and κ and power-law from [Pandya et al. \(2016\)](#). The fit formulas for the κ coefficients are only valid for $\kappa < 7.5$, they do not recover the thermal DF in the limit of $\kappa \rightarrow \infty$.

2.4 Cross-sections

The cross-section for an IC scattering is dependent on the local electron population, both the energy budget as well as the shape of the distribution. The cross-section is given by

$$\alpha_\nu = n_m \sigma_h \quad (17)$$

where σ_h is defined as the ‘‘hot cross section’’,

$$\sigma_h = \frac{1}{n_e} \int d^3p \frac{dn_e}{d^3p} (1 - \mu_e \beta_e) \sigma, \quad (18)$$

where n_e is the number density of electrons, $\frac{dn_e}{d^3p}$ is the electron distribution function, μ_e is the cosine of the angle between the superphoton momentum and the electron momentum, and β_e is the electron speed in the plasma frame, and σ the Klein-Nishina total cross-section.

From the cross-section the code computes the scattering opacity τ_s , via $\tau_s = \alpha_s r_g h / (m_e c^2) \Delta\lambda$, where α_s is the extinction coefficient given by $\alpha_s = n_e \sigma_h$. The total probability for a scattering event is then given by $p = 1 - e^{-b\tau_s}$, where b is a bias factor that enhances the scattering probability, as introduced in [Dolence et al. \(2009\)](#). This bias is then counteracted by splitting the scattered superphoton into an upscattered superphoton with weight bw and an unscattered remnant superphoton with weight $(1-b)w$. In this work, `κmonty` only exploits the original `grmonty` bias function given by $b = \Theta_e / \langle \Theta_e \rangle$, where $\langle \Theta_e \rangle$ is the volume averaged dimensionless electron temperature. More fine-tuned bias functions, such as the one in `igrmonty` ([Wong et al. 2022](#)), are not explored since the main focus of this work is the numerical algorithms for non-thermal DF sampling.

2.5 Sampling routines

The outcome of a Compton scattering event between a superphoton, and an electron depends on the superphoton’s wavevector and the electron’s four-velocity. The electrons are, in the case of GRMHD models, coupled to the plasma parameters of the protons, which are approximated by a fluid description. We, therefore, only know ensemble averages. To be able to select a single electron, we need a sampling algorithm that, given a set of plasma variables, draws a γ factor based on the chosen DF, in the original `grmonty`, the procedure from [Canfield et al. \(1987\)](#) is used for the MJ DFs. Therefore, only new samplers for the κ -DF and power law-DF are needed.

2.5.1 A semi-analytical sampling routine for the κ distribution function

For the κ -DF, we will generalise the procedure from [Canfield et al. \(1987\)](#) for the κ -distribution function. The relativistic κ -distribution function as function of velocity $\beta = \frac{v}{c}$ is given by

$$f_\kappa(\beta, w) = N w \beta^2 \gamma^5 \left(1 + \frac{\gamma - 1}{\kappa w}\right)^{-\kappa-1}, \quad (19)$$

with $\gamma = (1 - \beta^2)^{-1/2}$.

To sample electrons based on this distribution function, we derive a Monte Carlo-based scheme. We first introduce a random variable y that is coupled to γ and w

$$y^2 = \frac{\gamma - 1}{w}, \quad (20)$$

and transform our probability density function (pdf) accordingly

$$f_\kappa(y, w) = f_\kappa(\beta, w) \frac{\partial \beta}{\partial y}, \quad (21)$$

$$f_\kappa(y, w) = N w \sqrt{2w} y^2 \sqrt{1 + 0.5w y^2 (1 + w y^2)} \left(1 + \frac{y^2}{\kappa}\right)^{-\kappa-1}. \quad (22)$$

Following the procedure by [Canfield et al. \(1987\)](#), we can split our pdf into a series of pdfs after multiplying with

$$1 = \frac{1 + \sqrt{0.5wy}}{1 + \sqrt{0.5wy}}, \quad (23)$$

to obtain

$$f_\kappa(y, w) = \sqrt{2wy^2} \left(1 + \sqrt{0.5wy}\right) (1 + wy^2) \times \left(1 + \frac{y^2}{\kappa}\right)^{-\kappa-1} Nw \frac{\sqrt{1 + 0.5wy^2}}{1 + \sqrt{0.5wy}}, \quad (24)$$

this can be rewritten as

$$f_\kappa(y, w) = \left(y^2 + \sqrt{0.5wy^3} + wy^4 + w\sqrt{0.5wy^5}\right) \times \left(1 + \frac{y^2}{\kappa}\right)^{-\kappa-1} Nw\sqrt{2w} \frac{\sqrt{1 + 0.5wy^2}}{1 + \sqrt{0.5wy}}. \quad (25)$$

We can now identify two different functions that are the core of the sampling routine, a rejection function $H_3(w, y)$ and a sampling function $G_3(w, y)$ such that

$$f_\kappa(y, w) = G_3(w, y)H_3(w, y). \quad (26)$$

The sampling function is given by

$$G_3(w, y) = \sum_{j=3}^6 \pi_j(w)g_j(y), \quad (27)$$

and consists of a series of sample coefficients $g_j(y)$ and probability coefficients $\pi_j(w)$. The sampling coefficients are given by

$$g_j(y) \equiv \frac{y^{j-1}}{n_j} \left(1 + \frac{y^2}{\kappa}\right)^{-\kappa-1} \quad (28)$$

where n_j is a normalisation constant obtained by integrating

$$\int_0^\infty n_j g_j(y) dy = n_j. \quad (29)$$

Performing these four integrals, we get

$$n_3 = \frac{\sqrt{\kappa}\sqrt{\pi}\Gamma(-\frac{1}{2} + \kappa)}{4\Gamma(\kappa)}, \quad (30)$$

$$n_4 = \frac{\kappa}{2(-1 + \kappa)}, \quad (31)$$

$$n_5 = \frac{3\kappa^{3/2}\sqrt{\pi}\Gamma(-\frac{3}{2} + \kappa)}{8\Gamma(\kappa)}, \quad (32)$$

$$n_6 = \frac{\kappa^2}{2 - 3\kappa + \kappa^2}, \quad (33)$$

where $\Gamma(x)$ is the Gamma function. The analytical solutions for the normalisations are only valid in the case that $\kappa > 2$. The probability coefficients are given by

$$\pi_3(w) = \frac{n_3}{S_3(w)} \quad (34)$$

$$\pi_4(w) = \frac{n_4\sqrt{0.5w}}{S_3(w)} \quad (35)$$

$$\pi_5(w) = \frac{n_5w}{S_3(w)} \quad (36)$$

$$\pi_6(w) = \frac{n_6w\sqrt{0.5w}}{S_3(w)} \quad (37)$$

with

$$S_3(w) = n_3 + n_4\sqrt{0.5w} + n_5w + n_6w\sqrt{0.5w}. \quad (38)$$

The rejection function $H_3(w, y)$ is then defined as

$$H_3(w, y) = \frac{Nt\sqrt{2w} \sqrt{1 + 0.5wy^2}}{S_3(w) (1 + \sqrt{0.5wy})}. \quad (39)$$

The rejection criterion is then, similarly to [Canfield et al. \(1987\)](#),

$$h(w, y) = \frac{\sqrt{1 + 0.5wy^2}}{1 + \sqrt{0.5wy}}. \quad (40)$$

The rejection criterion can be generalised even more when one also wants to add an exponential cutoff to the κ -distribution function,

$$f_{\kappa, \gamma_{\text{cutoff}}}(\gamma) = f_\kappa(\gamma)e^{-\frac{\gamma}{\gamma_{\text{cutoff}}}}. \quad (41)$$

We can contract the exponential cutoff into the rejection criterion. Since if we encounter a large value of γ , it will decrease the likelihood of being accepted by the sampling routine,

$$h(w, y) = \frac{\sqrt{1 + 0.5wy^2}}{1 + \sqrt{0.5wy}} e^{-\frac{wy^2}{\gamma_{\text{cutoff}}}}. \quad (42)$$

The procedure for sampling the κ distribution function is, therefore

- (i) Draw a random number x_1
- (ii) If $x_1 < \pi_j$
- (iii) Find y according to $g_j(y)$
- (iv) Draw a random number x_2
- (v) Accepted y when $x_2 < h(w, y)$

This rejection constraint is, as mentioned in [Canfield et al. \(1987\)](#), very efficient because for large values of w or small values of w , $h(w, y)$ asymptotes to one.

The last step in this derivation of the sampling routine is to find a procedure for the third step, find y according to $g_j(y)$. In the case of a thermal distribution function, the $g_j(y)$ are χ^2 functions that can be sampled with standard `gsl` library functions. In the case of the κ -distribution function, this is less straightforward. To sample $g_j(y)$, we make use of the fact that the cumulative distribution functions (CDF) belonging to the pdfs $g_j(y)$ are monotonically increasing functions between zero and one. These CDFs can be obtained by integrating $g_j(y)$ from zero to y ,

$$F_j(y) = \int_0^y g_j(y) dy. \quad (43)$$

Performing these four integrals result in

$$F_3(y) = -\frac{\sqrt{\kappa} \left(\frac{y^2 + \kappa}{\kappa}\right)^{-\kappa} \Gamma(\kappa)}{\sqrt{\pi}y\Gamma(\kappa + \frac{3}{2})} \times [-\kappa_2 F_1(1, -\kappa - 1/2; 1/2; -y^2/\kappa) + y^2(2\kappa + 1) + \kappa], \quad (44)$$

$$F_4(y) = 1 - (y^2 + 1) \left(\frac{y^2 + \kappa}{\kappa}\right)^{-\kappa}, \quad (45)$$

$$F_5(y) = \frac{\left(\frac{y^2+\kappa}{\kappa}\right)^{-\kappa} \Gamma(\kappa)}{3\sqrt{\pi}y\sqrt{\kappa}\Gamma\left(\kappa + \frac{3}{2}\right)} [3\kappa^2 ({}_2F_1(1, -\kappa - 1/2; 1/2; -y^2/\kappa) - 1) + (1 - 4\kappa^2)y^4 - 3\kappa(2\kappa + 1)y^2], \quad (46)$$

$$F_6(y) = \frac{(y^4 - (y^4 + 2y^2 + 2)\kappa) \left(\frac{y^2+\kappa}{\kappa}\right)^{-\kappa}}{2\kappa} + 1, \quad (47)$$

where ${}_2F_1$ is the second-order hypergeometrical function of the first kind. We can then find an y by using an inverse transform sampling method,

- (i) draw a number u from a uniform distribution $[0, 1]$
- (ii) solve such that $F_j(y) = u$, where $F_j(y)$ is the cumulative distribution function of $g_j(y)$
- (iii) y is sampled according to $g_j(y)$

To solve step two, we implemented a Brent root-finding algorithm.

For the implementation of the algorithm, special attention has to be paid to the hypergeometrical functions encountered in the CDFs. For negative integer values of the arguments of the hypergeometrical function, it is impossible to use the series expansion form, as implemented in the `gsl` library. We, therefore, pre-computed a table of the hypergeometrical function as a function of κ and y with `Mathematica`, which is read in by `κmonty`. The resulting table is then interpolated with a first-order interpolation scheme.

2.5.2 The $\kappa \rightarrow \infty$ limit

In the case that $\kappa \rightarrow \infty$ we expect our derived sampler to recover the original sampler by [Canfield et al. \(1987\)](#).

First, we check that eqn. ?? recovers the pdfs in [Canfield et al. \(1987\)](#) by taking $\lim_{\kappa \rightarrow \infty} g_j(y)$, resulting in,

$$g_3(y) = \lim_{\kappa \rightarrow \infty} \frac{y^2}{n_3} \left(1 + \frac{y^2}{\kappa}\right)^{-\kappa-1} = \frac{y^2}{n_3} e^{-y^2} \quad (48)$$

$$g_4(y) = \lim_{\kappa \rightarrow \infty} \frac{y^3}{n_4} \left(1 + \frac{y^2}{\kappa}\right)^{-\kappa-1} = \frac{y^3}{n_4} e^{-y^2} \quad (49)$$

$$g_5(y) = \lim_{\kappa \rightarrow \infty} \frac{y^4}{n_5} \left(1 + \frac{y^2}{\kappa}\right)^{-\kappa-1} = \frac{y^4}{n_5} e^{-y^2} \quad (50)$$

$$g_6(y) = \lim_{\kappa \rightarrow \infty} \frac{y^5}{n_6} \left(1 + \frac{y^2}{\kappa}\right)^{-\kappa-1} = \frac{y^5}{n_6} e^{-y^2}. \quad (51)$$

Here we used that $\lim_{\kappa \rightarrow \infty} (1 + y/\kappa)^{-(\kappa+1)} = e^{-y}$. The resulting $g_j(y)$ in this limit are consistent with [Canfield et al. \(1987\)](#).

Secondly, we check $\lim_{\kappa \rightarrow \infty} n_j(y)$, which are given by

$$n_3 = \lim_{\kappa \rightarrow \infty} \frac{\sqrt{\kappa}\sqrt{\pi}\Gamma(-\frac{1}{2} + \kappa)}{4\Gamma(\kappa)} = \sqrt{\pi}/4, \quad (52)$$

$$n_4 = \lim_{\kappa \rightarrow \infty} \frac{\kappa}{2(-1 + \kappa)} = 1/2, \quad (53)$$

$$n_5 = \lim_{\kappa \rightarrow \infty} \frac{3\kappa^{3/2}\sqrt{\pi}\Gamma(-\frac{3}{2} + \kappa)}{8\Gamma(\kappa)} = 3\sqrt{\pi}/8, \quad (54)$$

$$n_6 = \lim_{\kappa \rightarrow \infty} \frac{\kappa^2}{2 - 3\kappa + \kappa^2} = 1. \quad (55)$$

Here we use that $\lim_{\kappa \rightarrow \infty} \kappa^{n/2}\Gamma(-n/2 + \kappa)/\Gamma(\kappa) = 1$. The resulting formulas are consistent with [Canfield et al. \(1987\)](#).

Our last test is to check the rejection criterion, which is already in the same form and is equal to the one by [Canfield et al. \(1987\)](#) in the case that $\lim_{\kappa \rightarrow \infty} w = \Theta_e$, which is the case if $w = \frac{\kappa-3}{\kappa}\Theta_e$.

2.5.3 A numerical sampling routine for the κ distribution function

We also implemented a more mundane rejection sampling method for drawing electrons from the κ distribution. This implementation can be found in the public code `igrmonty`³ as well as in `κmonty`. The expression $\partial f_\kappa/\partial \gamma = 0$ is solved for γ , hereafter γ_{\max} . Fiducial γ are then drawn uniformly in log space between

$$\gamma_{\min,} = \text{MAX}(1, 0.01 \times \Theta_e) \quad (56)$$

$$\gamma_{\max,} = \text{MAX}(100, 1000 \times \Theta_e) \quad (57)$$

where these parameters are chosen to ensure both accuracy and computational efficiency for all Θ_e . New γ are drawn until the condition $\gamma f_\kappa(\gamma)/\gamma_{\max} f_\kappa(\gamma_{\max}) > \text{rand}$, where rand is a uniformly distributed random number in the range $[0, 1]$ and the extra factors of γ arise from drawing fiducial γ uniformly in log space.

This procedure generalises to any realistic electron distribution function, including the MJ distribution, but also, e.g., anisotropic DFs, DF based on charged test particles in MHD, or DFs based on first-principle PIC simulations. Compared to the [Canfield et al. \(1987\)](#) prescription for sampling MJ, this rejection sampling approach leads to only modestly ($\sim 20\%$) slower calculation wallclock times.

2.5.4 Power-law distribution

For the power-law distribution function, the procedure is much more trivial. The cumulative distribution function is, in this case, given by

$$F(\gamma) = \int_{\gamma_{\min}}^{\gamma} \frac{(p-1)\gamma^{-p}}{(\gamma_{\min}^{1-p} - \gamma_{\max}^{1-p})} d\gamma = \frac{(\gamma_{\min}^{1-p} - \gamma^{1-p})}{(\gamma_{\min}^{1-p} - \gamma_{\max}^{1-p})}. \quad (58)$$

Since this CDF can be inverted analytically, we can use an inverse sampling method. We first pick a random number x between zero and one, and γ can then be found by computing the inverse of eqn. 58 and setting $F(\gamma) = x$,

$$\gamma = ((1-x)\gamma_{\min}^{1-p} + x\gamma_{\max}^{1-p})^{1/(1-p)}. \quad (59)$$

2.6 Interface with BHAC

The Black Hole Accretion Code (BHAC) ([Porth et al. 2017](#); [Olivares et al. 2019](#)) is a finite volume code that solves the covariant GRMHD equation using a 3+1 split. The code is capable of using AMR grids that, during runtime, based on user-defined criteria, can refine or derefine the grid. BHAC outputs the GRMHD data in an octree structure. We fully interfaced `κmonty` to this data format similarly to [Davelaar et al. \(2019\)](#), and made `κmonty` capable of initialising superphotons and performing IC in a non-uniform grid.

³ <https://github.com/AFD-Illinois/igrmonty>

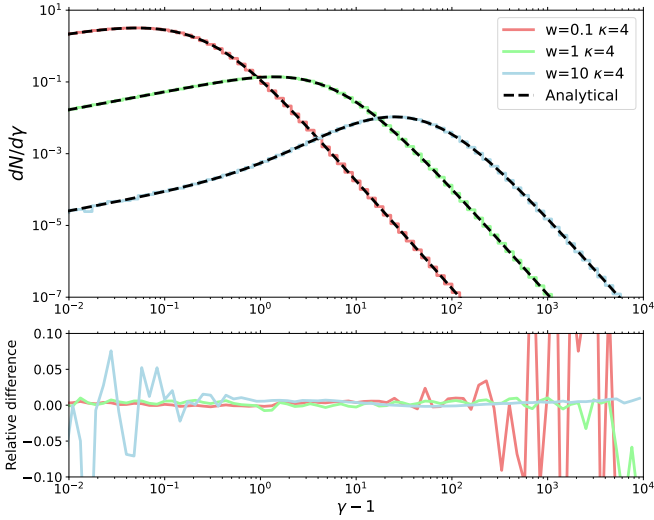


Figure 2. Output of the κ sampler compared to the analytical form for: $w = 0.1$ (red), $w = 1.0$ (green) and $w = 10$ (blue). All three cases use $\kappa = 4.0$. The majority of the DF from the sampler shows almost perfect agreement with respect to the exact form. Only at a low or high Lorentz factor the error increases for the $w = 10$ and $w = 0.1$ cases, respectively. This is caused by the MC nature of our sampler, which makes regions with small electron number density harder to sample due to MC noise.

3 CODE VERIFICATION

To verify our implementation of the described methods, we performed extensive code tests. In this section, we describe the performed tests and discuss the results.

3.1 Sampling routines

We first tested the sampling routines by computing κ -distribution functions for three values of $w = [0.1, 1, 10]$ and $\kappa = 4$. This is done by drawing 10^9 electrons and comparing the resulting distribution with the analytical form. The results of this are shown in figure 2. Overall the relative difference between the exact form and the distribution is close to 0% for all values of w , except for γ values close to one for $w = 10$, or large γ values in the case of $w = 0.1$. For these γ values, the distribution functions have a small population of electrons, which are therefore dominated by MC noise. Similarly, for the power-law distribution, we computed distribution for three values of the power-law index, $p = [3, 4, 5]$ and $\gamma_{\min} = 3.5$, and $\gamma_{\max} = 10^4$. The results of this are shown in figure 3. We find good agreement between the analytical form and the output of our sampler, and large deviations from 0% are only found in regions with low electron number densities, e.g., large γ values.

3.2 Uniform sphere test

To test the implementation of both the emission coefficients and the scattering kernel, we designed a simple one-zone model that we will use to compare κ monty with the ray

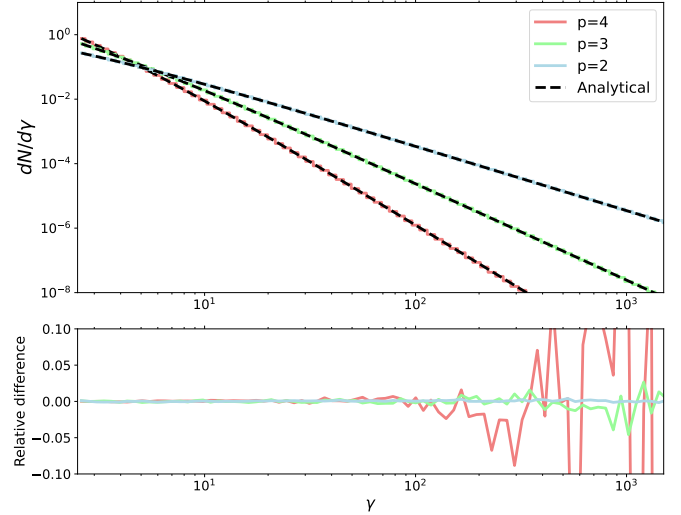


Figure 3. Output of the power-law sampler compared to the analytical form, $p = 4.0$ (red), $p = 3.0$ (green), and $p = 2.0$ (blue). For all three cases we set $\gamma_{\min} = 1.0$ and $\gamma_{\max} = 10^3$. The deviation between the sampler and the exact form is for almost the entire range less than 1%, except for large γ values, due to the steep power-law populating the high end of the DF is affected by MC noise.

tracing codes **RAPTOR**⁴ and **ipole-IL** and cross-compare the semi-analytical and numerical samplers in κ monty and **igrmonty**. The one-zone model is an isothermal sphere with a uniform density profile embedded in a uniform vertical magnetic field in flat spacetime. We solve the problem in spherical polar coordinates; the non-zero metric terms are given by

$$g_{tt} = -1 \tag{60}$$

$$g_{rr} = 1 \tag{61}$$

$$g_{\theta\theta} = r^2 \tag{62}$$

$$g_{\phi\phi} = r^2 \sin^2(\theta). \tag{63}$$

The plasma variables are given by,

$$\rho = \rho_0 \tag{64}$$

$$\Theta_e = \Theta_{e,0} \tag{65}$$

$$B^t = 0. \tag{66}$$

$$B^r = B_0 \cos \theta \tag{67}$$

$$B^\theta = -B_0 \sin \theta / r \tag{68}$$

$$B^\phi = 0. \tag{69}$$

The solution is specified by constants ρ_0 , R_0 , $\Theta_{e,0}$, and B_0 , along with an outer boundary to the domain R_{out} . ρ_0 is given in terms of a characteristic Thomson depth τ_0 :

$$\rho_0 = \frac{\tau_0}{\sigma_T R_0 \mathcal{L} \mathcal{N}} \tag{70}$$

where \mathcal{L} is the code length unit conversion and \mathcal{N} is the electron number density unit conversion. B_0 is expressed in

⁴ <https://github.com/jordydavelaar/raptor>

terms of the plasma β at $r = 0$, β_0 :

$$B_0 = \sqrt{\frac{2P_g}{\beta_0}} \quad (71)$$

where P_g is the gas pressure. We set the adiabatic index to $\hat{\gamma}_{\text{adiab}} = 13/9$, and the ratio between the proton and electron temperature is set to be $T_{\text{rat}} = 3.0$.

3.2.1 Comparison with RAPTOR

To check whether the implementation of the emission coefficients is correct, we compute the SED without Compton scattering of the uniform sphere with κmonty and RAPTOR. RAPTOR (Bronzwaer et al. 2018; Davelaar et al. 2018a; Bronzwaer et al. 2020) is a General Relativistic Ray tracing code that solves the covariant radiation transport equation in curved spacetime. GRRT methods are intrinsically different from MC methods since they use bundles of rays. This makes them ideal for computing synthetic images since only a small portion of the sky is covered by a camera. The camera consists of pixels, and every pixel is assigned an initial wavevector used to solve the geodesic equation backwards in time. Along these geodesics, the unpolarised radiation transport equation is solved.

The setup and code-specific parameters for both κmonty as well as RAPTOR are shown in Table 1. The results of this test can be seen in Figure 4. All three cases show minor discrepancies between the two codes except for the low-frequency part of the spectrum, which is dominated by MC noise. The thermal case shows deviations at the highest frequencies as well. The source becomes optically thin at these frequencies, and the emission region shrinks. The electrons responsible for this emission are at the exponential tail of the distribution functions, affecting the sampling.

3.2.2 Comparison with ipole-IL

As an additional independent test to validate both κmonty as well as RAPTOR, we also cross-compared the output of κmonty with the ipole-IL ray tracing code (Mościbrodzka and Gammie 2018; Wong et al. 2022). This test is identical to the test with RAPTOR presented in the previous subsection. The result can be seen in Figure 5, and the agreement between the two codes is identical to the test with RAPTOR.

3.2.3 Compton Scattering test

To test the implementation of the non-thermal DFs within the Compton scattering module, we cross-compared a semi-analytical implementation with a numerical one in igr-monty . The camera is positioned at a distance of $10^4 \mathcal{L}$, and we compute spectra for three inclinations $30^\circ, 60^\circ, 90^\circ$. The full set of parameters is similar to the ones shown in Table 1, except that $N_\theta = 3, N_\phi = 1$. And we use folding around the equator, meaning bins in the half-sphere above and below the equator are averaged to increase statistics.

The results of this comparison can be seen in Figure 6. There is clear consistency between the two methods, with a relative difference of less than 1% for most of the SED. The MC noise grows at high frequencies due to the low probability of double-scattering events. To test the convergence of

Source parameters	value
Distance	8.5 kpc
M_{BH}	$4.1 \times 10^6 M_\odot$
Uniform sphere parameters	
R_0	100
τ_0	10^{-5}
$\Theta_{e,0}$	10
β_0	20
GRMHD parameters	
R_{max}	40
\mathcal{M}	10^{19} g
T_{rat}	3.0
DF parameters	
$\kappa(p)$	4.0 (3.0)
w	$\Theta_e \frac{\kappa-3}{\kappa}$
T_{ratio}	3.0
ν_{cutoff}	5×10^{13} Hz
γ_{cutoff}	10^3
γ_{min}	25
γ_{max}	10^7
Code parameters κmonty	
ν_{min}	10^9 Hz
ν_{max}	10^{16} Hz
N_θ	180
N_ϕ	90
RMAX	$10^4 r_g$
equatorial folding	no
Code parameters RAPTOR and ipole-IL	
field of view	$300 r_g$
pixels	512^2
r_{cam}	$10^4 r_g$
i_{cam}	90°

Table 1. Code and test parameters for all tests described in this paper.

this test, we performed multiple runs with different amounts of initial superphotons. The convergence can be seen in the right panel of Figure 6. There is a clear \sqrt{N} convergence visible, as would be expected of a Monte Carlo code.

3.3 GRMHD test

A more challenging test is performed by comparing the synchrotron part of the SED between κmonty and RAPTOR computed from a snapshot of a GRMHD simulation. The simulation, in CKS coordinates, is the same as that presented in Davelaar et al. (2019); Olivares et al. (2019). The initial condition of this simulation is a Fishbone and Moncrief (1976) torus with black hole spin parameter $a_* = 15/16$, inner radius $6 GM/c^2$, pressure maximum at $12 GM/c^2$, and adiabatic index $\hat{\gamma} = 4/3$. The initial magnetic field profile is a single poloidal loop that follows isocontours of the density profile. The initial torus is weakly magnetised and set by the ratio between the maximum magnetic pressure $P_{\text{mag,max}}$ and maximum gas pressure P_{max} and is set to be $P_{\text{max}}/P_{\text{mag,max}} = 100$.

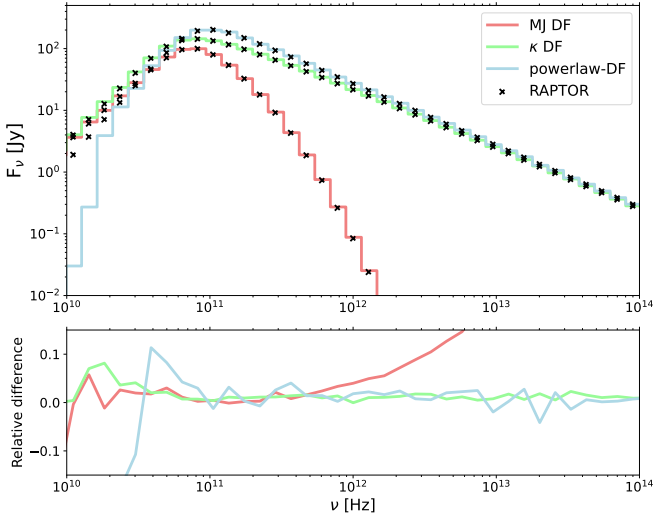


Figure 4. Comparison between *κmonty* and *RAPTOR* for the uniform sphere test. Top panel: spectra for MJ-DF (red), *κ*-DF (green), and power-law DF (blue) for *κmonty*, black crosses data point from *RAPTOR*. Bottom panel: the relative difference between the three DFs. The relative error is around 1% for the majority of the SED. In the thermal case, at high frequency, the error grows. This is caused by a quickly shrinking emission region size, making sampling more difficult. All three models show slightly more noise at low frequencies due to the larger optical thickness. More superphotons are absorbed, which makes convergence more difficult compared to the optically thin part of the spectrum.

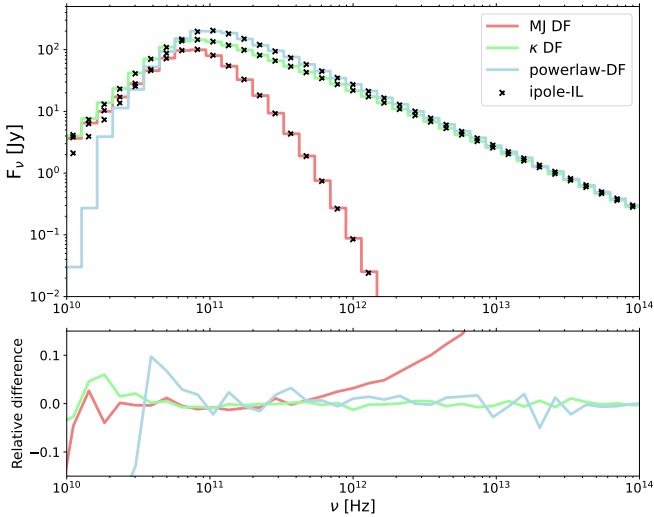


Figure 5. Comparison between *κmonty* and *ipole-IL* for the uniform sphere test. Identical results compared to Figure 4

Since the GRMHD simulation we used does not include electron thermodynamics, we use a parameterisation for the electron temperature

$$\Theta_e = \frac{U(\hat{\gamma} - 1)m_p}{\rho m_e (T_{\text{rat}} + 1)}, \quad (72)$$

where U is the internal energy, m_p the proton mass, m_e the electron mass, and T_{rat} the ratio between the proton to electron temperature which we set to $T_{\text{rat}} = 3.0$. To impose charge neutrality of the plasma, we set the electron number density equal to the proton number density.

The GRMHD simulation is scale-free to convert from code to c.g.s. units. Besides the aforementioned length and time unit, also a mass unit \mathcal{M} is needed. The length and time units are given by the black hole length and gravitational timescales, $r_g = GM_{\text{BH}}/c^2$ and $t_g = r_g/c$, while the mass unit sets the energy content of the simulation and is tightly related to the mass accretion rate via $\dot{M} = \dot{M}_{\text{sim}}\mathcal{M}/\mathcal{T}$. To convert the plasma variable to c.g.s. units the following conversion factors are used: $\rho_0 = \mathcal{M}/\mathcal{L}^3$, $u_0 = \rho_0 c^2$, and $B_0 = c\sqrt{4\pi\rho_0}$.

The test-specific parameters for the camera, DF, and GRMHD parameters can be seen in Table 1. Only the inner $40 r_g$ of the GRMHD domain is used to limit the field of view needed and speed up the convergence of the MC solution.

The results of this test can be seen in Figure 7. For all three DFs, the error is close to 1% in most frequency bins. For the thermal case at high frequency, the error grows at high frequencies, similar to the uniform sphere test. All three DFs show less agreement at lower frequencies (around 10^{10} Hz), due to opacity effects.

4 CODE PERFORMANCE AND AVAILABILITY

Since the convergence of a Monte-Carlo simulation scales with \sqrt{N} , with N the amount of superphotons, it is computationally demanding to acquire a fully converged solution. To accelerate the convergence, *grmonty* was parallelized with *OpenMP*, allowing it to run on multiple cores on a single node. To improve our code performance even further, we parallelized *κmonty* with *MPI*, which allows us to run over many nodes. We identified two potential ways to *MPI* parallelize our computations. One could either distribute the GRMHD domain over all the available *MPI* processes and trace superphotons through the domain, this could lead to substantial communication overhead when superphotons leave/enter the domain of a processor, or would require a very labour intensive implementation where batched superphotons are send and received with non-blocking *MPI*. Alternatively, one could launch independent *MPI* instances that all have the full domain in memory and at termination, sum all the resulting spectra. The first option has the benefit that it is memory efficient. However, scaling is limited to the IO overhead as the domain per *MPI* instance gets smaller. The second option is more memory demanding but is trivial to implement and is easily scalable to large numbers of nodes as long as the domain fits within the memory per *MPI* task. A typical 256^3 simulations takes about five Gigabytes of memory, which allows for this implementation strategy, for high resolution simulations either the first method or a hydro *Openmp+MPI* implementation should be explored. For *κmonty*, we opted for the second parallelization strategy. In the remainder of this section, we test our implementation for scalability and performance.

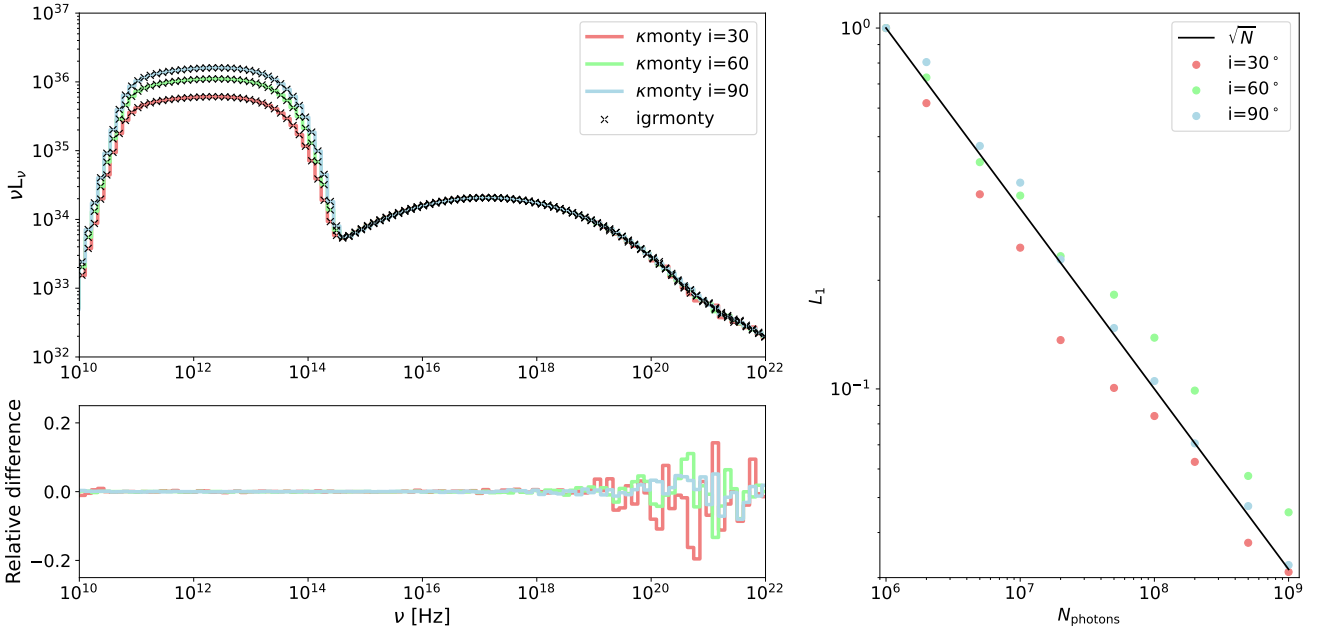


Figure 6. Comparison between the semi-analytical (κ monty) and numerical sampler (igrmonty) at three inclinations, top left: spectra at inclinations of 30° , 60° , and 90° . All three cases show consistent spectra with order 1% differences (bottom left). The MC noise grows at high frequencies due to the low probability of double-scattering events. Right: L_1 convergence of the comparison between the semi-analytical and numerical samplers. As expected of MC methods, a clear \sqrt{N} trend is visible.

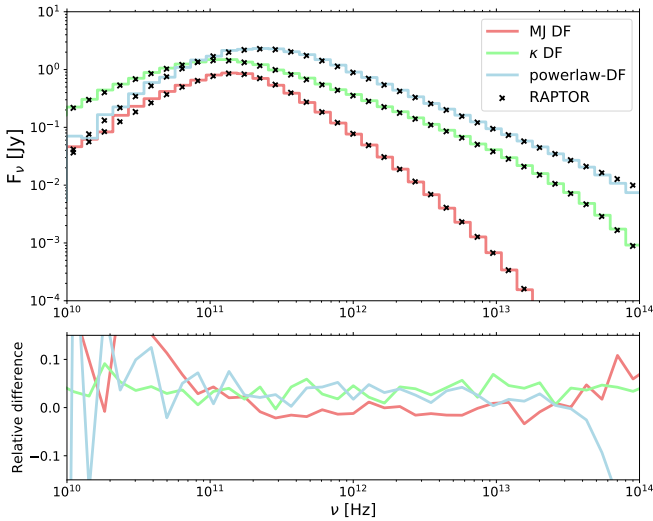


Figure 7. Comparison between RAPTOR and κ monty for the GRMHD test, left: Thermal DF, middle: κ -DF, right: power-law DF. Consistent with the uniform sphere test, the deviations are of the order of 1% per cent except for the high or low-frequency part of the spectrum.

The code is publicly available on GitHub⁵. To test the performance of κ monty we ran a BHAC MKS GRMHD snapshot with scattering for the κ -DF and thermal-DF. First,

we varied the number of initial superphotons to test for the solution's self-convergence. The resulting spectra for $N = (10^6, 10^7, 10^8, 10^9)$ can be seen in the left panel of Figure 8. The right panel shows the convergence rate, which shows a \sqrt{N} scaling. Secondly, we ran the code on varying amounts of nodes to test our code's scalability. For this test, we used nodes with 128 AMD Rome cores with a total processing power per node of 4.6 teraflops. We compiled the code with the intel compiler and standard intel optimization flags. We varied the number of nodes from 1 to 40 nodes. Again, we use the GRMHD setup with scattering and start the code with $N = 10^5$ superphotons per core. The scaling is shown in Figure 9, and shows an evident linear scaling. Overall we achieve a speed of a few thousand superphotons per second per core, although note that this highly depends on the problem, stepsize, and scattering opacity. The 40 nodes run achieves a speed of ten million superphotons per second. The difference between the thermal, power-law, and κ -DFs is negligible since the computational bottleneck is the handling of the non-uniform data structure and geodesic integration.

We also tested the performance of the semi-analytical samplers. We provide a stand-alone openmp accelerated code of the sampling routines on GitHub⁶. We ran the samplers on the same architecture as for the κ monty performance test. The κ -DF samples a few hundred thousand electrons per second per core, while the power-law and thermal DF samples around ten million electrons per second per core. Although the κ -DF is orders of magnitude slower, since it does not make use of heavily optimized gsl samplers, the routine

⁵ <https://github.com/jordydavelaar/kmonty>

⁶ <https://github.com/jordydavelaar/edf-samplers>

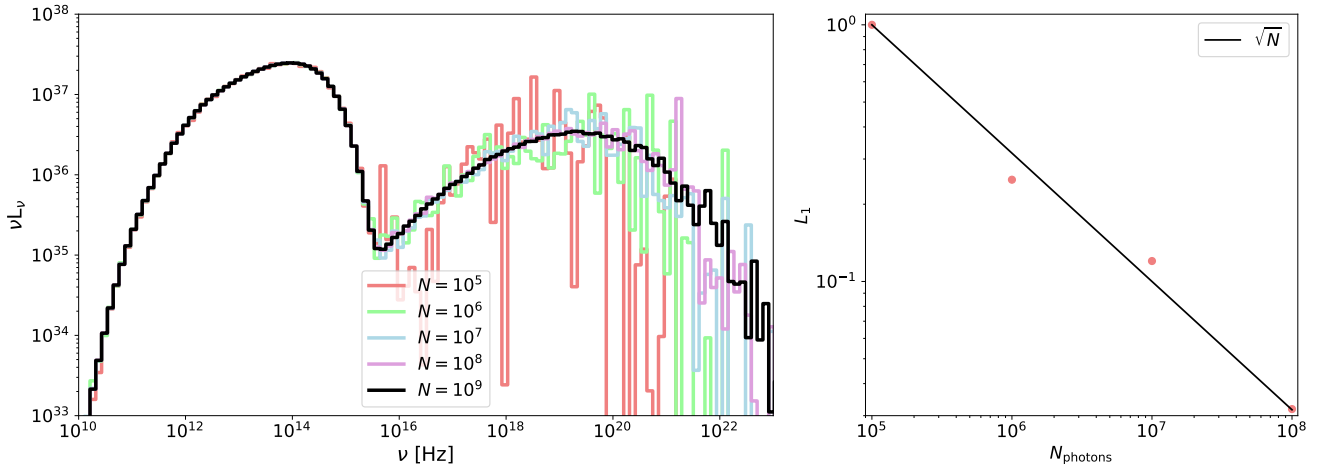


Figure 8. Self convergence of the spectra based on the GRMHD snapshot including Compton scattering, model uses the κ -DF. Left: spectra for $N = (10^5, 10^6, 10^7, 10^8, 10^9)$ superphotons. Right: self convergence of the solution with respect to the $N = 10^9$ superphotons run. An evident \sqrt{N} scaling is visible as expected for MC methods.

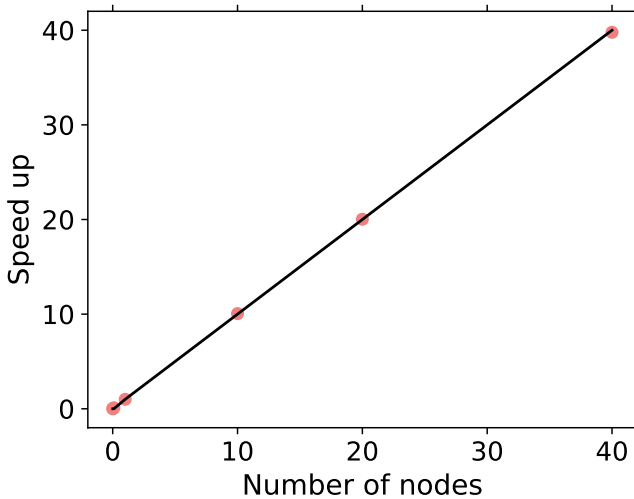


Figure 9. Scaling performance of the code for varying cores. We increased the amount of nodes from one to 40 nodes, each containing 128 cores, and computed the speed up. An evident linear scaling is visible in the red points, as the black line indicates perfect linear scaling.

is only called at most one or two times per superphoton, meaning the computational cost is negligible when used by *κmonty*.

5 CONCLUSION

We presented our new *κmonty* code. The code is an extension of *grmonty* and now includes κ and power-law distribution functions for both the radiative transfer coefficients and sampling routines. The code can also post-process the AMR data format of BHAC. We tested our sampling routines by comparing the numerical output to the analytical DFs.

We used a uniform isothermal sphere to test the implementations of the emission coefficients by comparing them with the ray-tracing code *RAPTOR*. We tested the full emission and scattering kernels by comparing them to an implementation of the kappa distribution in *igrmonty* that uses the numerical sampling routine. And finally, test the coupling to BHAC by comparing the synchrotron emission with *RAPTOR* by using a snapshot of a black hole simulation in Cartesian coordinates which uses AMR.

ACKNOWLEDGEMENTS

The authors thank Oliver Porth, Sasha Philippov, Jeremy Schnittman, and Chi-kwan Chan for valuable discussions and feedback on the project. JD is supported by NASA grant NNX17AL82G and a Joint Columbia/Flatiron Postdoctoral Fellowship. Research at the Flatiron Institute is supported by the Simons Foundation. GNW is supported by the Taplin Fellowship. HO was supported by a Virtual Institute of Accretion (VIA) postdoctoral fellowship from the Netherlands Research School for Astronomy (NOVA). This work has been assigned a document release number LA-UR-23-21157. This work was partly funded by the ERC Synergy Grant “BlackHoleCam-Imaging the Event Horizon of Black Holes” (Grant 610058, Goddi et al. (2017)). The GRMHD simulations were performed on the Dutch National Supercomputing cluster Cartesius and are funded by the NWO computing grant 16431. This research has made use of NASA’s Astrophysics Data System.

Software: *python* (Oliphant 2007; Millman and Aivazis 2011), *scipy* (Jones et al. 2001), *numpy* (van der Walt et al. 2011), *matplotlib* (Hunter 2007), *RAPTOR* (Bronzwaer et al. 2018, 2020).

DATA AVAILABILITY

The data underlying this article will be shared on reasonable request to the corresponding author.

REFERENCES

- Baganoff, F. K., Maeda, Y., Morris, M., Bautz, M., Brandt, W. N., Cui, W., Doty, J., Feigelson, E., Garmire, G., Pravdo, S., et al. (2003). Chandra x-ray spectroscopic imaging of sagittarius a* and the central parsec of the galaxy. *ApJ*, 591(2):891.
- Ball, D., Özel, F., Psaltis, D., and Chan, C.-k. (2016). Particle Acceleration and the Origin of X-Ray Flares in GRMHD Simulations of SGR A. *ApJ*, 826:77.
- Böttcher, M., Jackson, D. R., and Liang, E. P. (2003). Two-dimensional Monte Carlo/Fokker-Planck Simulations of Flares in Accretion Disk Corona Models. *apj*, 586:389–402.
- Böttcher, M. and Liang, E. P. (2001). Monte Carlo Simulations of Thermal-Nonthermal Radiation from a Neutron Star Magnetospheric Accretion Shell. *apj*, 552:248–258.
- Broderick, A. E., Narayan, R., Kormendy, J., Perlman, E. S., Rieke, M. J., and Doeleman, S. S. (2015). The Event Horizon of M87. *ApJ*, 805:179.
- Bronzwaer, T., Davelaar, J., Younsi, Z., Mościbrodzka, M., Falcke, H., Kramer, M., and Rezzolla, L. (2018). RAPTOR. I. Time-dependent radiative transfer in arbitrary spacetimes. *A&A*, 613:A2.
- Bronzwaer, T., Younsi, Z., Davelaar, J., and Falcke, H. (2020). RAPTOR II: Polarized radiative transfer in curved spacetime. *arXiv e-prints*, page arXiv:2007.03045.
- Canfield, E., Howard, W. M., and Liang, E. P. (1987). Inverse Comptonization by one-dimensional relativistic electrons. *ApJ*, 323:565–574.
- Chael, A. A., Narayan, R., and Sadowski, A. (2017). Evolving non-thermal electrons in simulations of black hole accretion. *MNRAS*, 470(2):2367–2386.
- Chan, C.-k., Liu, S., Fryer, C. L., Psaltis, D., Özel, F., Rockefeller, G., and Melia, F. (2009). MHD Simulations of Accretion onto Sgr A*: Quiescent Fluctuations, Outbursts, and Quasiperiodicity. *ApJ*, 701(1):521–534.
- Chan, C.-k., Psaltis, D., Özel, F., Medeiros, L., Marrone, D., Sadowski, A., and Narayan, R. (2015a). Fast Variability and Millimeter/IR Flares in GRMHD Models of Sgr A* from Strong-field Gravitational Lensing. *ApJ*, 812(2):103.
- Chan, C.-K., Psaltis, D., Özel, F., Narayan, R., and Sadowski, A. (2015b). The Power of Imaging: Constraining the Plasma Properties of GRMHD Simulations using EHT Observations of Sgr A*. *ApJ*, 799(1):1.
- Chatterjee, K., Markoff, S., Neilsen, J., Younsi, Z., Witzel, G., Tchekhovskoy, A., Yoon, D., Ingram, A., van der Klis, M., Boyce, H., Do, T., Haggard, D., and Nowak, M. (2020). General relativistic MHD simulations of non-thermal flaring in Sagittarius A*. *arXiv e-prints*, page arXiv:2011.08904.
- Cruz-Orsorio, A., Fromm, C. M., Mizuno, Y., Nathanail, A., Younsi, Z., Porth, O., Davelaar, J., Falcke, H., Kramer, M., and Rezzolla, L. (2022). State-of-the-art energetic and morphological modelling of the launching site of the M87 jet. *Nature Astronomy*, 6:103–108.
- Davelaar, J., Bronzwaer, T., Kok, D., Younsi, Z., Mościbrodzka, M., and Falcke, H. (2018a). Observing supermassive black holes in virtual reality. *arXiv e-prints*, page arXiv:1811.08369.
- Davelaar, J., Mościbrodzka, M., Bronzwaer, T., and Falcke, H. (2018b). General relativistic magnetohydrodynamical κ -jet models for Sagittarius A*. *A&A*, 612:A34.
- Davelaar, J., Olivares, H., Porth, O., Bronzwaer, T., Janssen, M., Roelofs, F., Mizuno, Y., Fromm, C. M., Falcke, H., and Rezzolla, L. (2019). Modeling non-thermal emission from the jet-launching region of M 87 with adaptive mesh refinement. *arXiv e-prints*, page arXiv:1906.10065.
- Decker, R. B. and Krimigis, S. M. (2003). Voyager observations of low-energy ions during solar cycle 23. *Advances in Space Research*, 32:597–602.
- Dolence, J. C., Gammie, C. F., Mościbrodzka, M., and Leung, P. K. (2009). grmonty: A Monte Carlo Code for Relativistic Radiative Transport. *ApJS*, 184:387–397.
- Dolence, J. C., Gammie, C. F., Shiokawa, H., and Noble, S. C. (2012). Near-infrared and X-Ray Quasi-periodic Oscillations in Numerical Models of Sgr A*. *apjl*, 746:L10.
- Eckart, A., Baganoff, F., Morris, M., Bautz, M., Brandt, W. N., Garmire, G., Genzel, R., Ott, T., Ricker, G., Straubmeier, C., et al. (2004). First simultaneous nir/x-ray detection of a flare from sgr a. *A&A*, 427(1):1–11.
- EHT Collaboration et al. (2019a). *ApJL*. 875, L1 (Paper I).
- EHT Collaboration et al. (2019b). *ApJL*. 875, L5 (Paper V).
- Event Horizon Telescope Collaboration (2022). First Sagittarius A* Event Horizon Telescope Results. V. Testing Astrophysical Models of the Galactic Center Black Hole. *ApJ*, 930(2):L16.
- Fishbone, L. G. and Moncrief, V. (1976). Relativistic fluid disks in orbit around Kerr black holes. *The Astrophysical Journal*, 207:962–976.
- Fromm, C. M., Cruz-Orsorio, A., Mizuno, Y., Nathanail, A., Younsi, Z., Porth, O., Olivares, H., Davelaar, J., Falcke, H., Kramer, M., and Rezzolla, L. (2022). Impact of non-thermal particles on the spectral and structural properties of M87. *A&A*, 660:A107.
- Goddi, C., Falcke, H., Kramer, M., Rezzolla, L., Brinkerink, C., Bronzwaer, T., Davelaar, J. R. J., Deane, R., de Laurentis, M., Desvignes, G., Eatough, R. P., Eisenhauer, F., Fraga-Encinas, R., Fromm, C. M., Gillessen, S., Grenzebach, A., Issaoun, S., Janßen, M., Konoplya, R., Krichbaum, T. P., Laing, R., Liu, K., Lu, R. S., Mizuno, Y., Mościbrodzka, M., Müller, C., Olivares, H., Pfuhl, O., Porth, O., Roelofs, F., Ros, E., Schuster, K., Tilanus, R., Torne, P., van Bemmell, I., van Langevelde, H. J., Wex, N., Younsi, Z., and Zhidenko, A. (2017). Black-HoleCam: Fundamental physics of the galactic center. *International Journal of Modern Physics D*, 26:1730001–239.
- Harris, D. E., Cheung, C. C., Stawarz, L., Biretta, J. A., and Perlman, E. S. (2009). Variability Timescales in the M87 Jet: Signatures of E^2 Losses, Discovery of a Quasi Period in HST-1, and the Site of TeV Flaring. *ApJ*, 699(1):305–314.
- Hunter, J. D. (2007). Matplotlib: A 2D Graphics Environment. *Computing in Science and Engineering*, 9:90–95.
- Jones, E., Oliphant, T., Peterson, P., et al. (2001). SciPy: Open source scientific tools for Python. [Online].
- Kerr, R. P. (1963). Gravitational Field of a Spinning Mass as an Example of Algebraically Special Metrics. *Phys. Rev. Lett.*, 11:237–238.
- Kunz, M. W., Stone, J. M., and Quataert, E. (2016). Magnetorotational Turbulence and Dynamo in a Collisionless Plasma. *Physical Review Letters*, 117(23):235101.
- Laurent, P. and Titarchuk, L. (1999). The Converging Inflow Spectrum Is an Intrinsic Signature for a Black Hole: Monte Carlo Simulations of Comptonization on Free-falling Electrons. *apj*, 511:289–297.
- Leung, P. K., Gammie, C. F., and Noble, S. C. (2011a). Numerical Calculation of Magnetobremstrahlung Emission and Absorption Coefficients. *ApJ*, 737:21.
- Leung, P. K., Gammie, C. F., and Noble, S. C. (2011b). Numerical Calculation of Magnetobremstrahlung Emission and Absorption Coefficients. *ApJ*, 737:21.
- Livadiotis, G. and McComas, D. J. (2013). Understanding kappa distributions: A toolbox for space science and astrophysics. *Space Science Reviews*, 175(1):183–214.
- Mao, S. A., Dexter, J., and Quataert, E. (2017). The impact of non-thermal electrons on event horizon scale images and

- spectra of Sgr A*. *MNRAS*, 466(4):4307–4319.
- Marshall, H. L., Miller, B. P., Davis, D. S., Perlman, E. S., Wise, M., Canizares, C. R., and Harris, D. E. (2002). A high-resolution x-ray image of the jet in m87. *ApJ*, 564(2):683–687.
- Millman, K. J. and Aivazis, M. (2011). Python for scientists and engineers. *Computing in Science & Engineering*, 13(2):9–12.
- Mościbrodzka, M. (2020). General relativistic polarized radiative transfer with inverse-Compton scatterings. *MNRAS*, 491(4):4807–4815.
- Mościbrodzka, M., Falcke, H., and Shiokawa, H. (2016). General relativistic magnetohydrodynamical simulations of the jet in M 87. *A&A*, 586:A38.
- Mościbrodzka, M. and Gammie, C. F. (2018). IPOLE - semi-analytic scheme for relativistic polarized radiative transport. *MNRAS*, 475(1):43–54.
- Mościbrodzka, M. A. (2022). Polarization-sensitive Compton Scattering by Accelerated Electrons. *ApJS*, 263(1):6.
- Narayan, R., Zhu, Y., Psaltis, D., and Sađowski, A. (2016). HEROIC: 3D general relativistic radiative post-processor with comptonization for black hole accretion discs. *mnras*, 457:608–628.
- Nathanail, A., Fromm, C. M., Porth, O., Olivares, H., Younsi, Z., Mizuno, Y., and Rezzolla, L. (2020). Plasmoid formation in global GRMHD simulations and AGN flares. *MNRAS*, 495(2):1549–1565.
- Oliphant, T. E. (2007). Python for scientific computing. *Computing in Science & Engineering*, 9(3):10–20.
- Olivares, H., Porth, O., Davelaar, J., Most, E. R., Fromm, C. M., Mizuno, Y., Younsi, Z., and Rezzolla, L. (2019). Constrained transport and adaptive mesh refinement in the Black Hole Accretion Code. *arXiv e-prints*, page arXiv:1906.10795.
- Özel, F., Psaltis, D., and Narayan, R. (2000). Hybrid Thermal-Nonthermal Synchrotron Emission from Hot Accretion Flows. *ApJ*, 541:234–249.
- Pandya, A., Zhang, Z., Chandra, M., and Gammie, C. F. (2016). Polarized Synchrotron Emissivities and Absorptivities for Relativistic Thermal, Power-law, and Kappa Distribution Functions. *ApJ*, 822:34.
- Perlman, E. S. and Wilson, A. S. (2005). The x-ray emissions from the m87 jet: Diagnostics and physical interpretation. *ApJ*, 627(1):140.
- Porth, O., Olivares, H., Mizuno, Y., Younsi, Z., Rezzolla, L., Mościbrodzka, M., Falcke, H., and Kramer, M. (2017). The black hole accretion code. *Computational Astrophysics and Cosmology*, 4:1.
- Prieto, M. A., Fernández-Ontiveros, J. A., Markoff, S., Espada, D., and González-Martín, O. (2016). The central parsecs of M87: jet emission and an elusive accretion disc. *MNRAS*, 457:3801–3816.
- Quataert, E. (2004). A Dynamical Model for Hot Gas in the Galactic Center. *ApJ*, 613(1):322–325.
- Ripperda, B., Bacchini, F., and Philippov, A. A. (2020). Magnetic Reconnection and Hot Spot Formation in Black Hole Accretion Disks. *ApJ*, 900(2):100.
- Ripperda, B., Liska, M., Chatterjee, K., Musoke, G., Philippov, A. A., Markoff, S. B., Tchekhovskoy, A., and Younsi, Z. (2022). Black Hole Flares: Ejection of Accreted Magnetic Flux through 3D Plasmoid-mediated Reconnection. *ApJ*, 924(2):L32.
- Ryan, B. R., Dolence, J. C., and Gammie, C. F. (2015). bhlight: General Relativistic Radiation Magnetohydrodynamics with Monte Carlo Transport. *apj*, 807:31.
- Schnittman, J. D. and Krolik, J. H. (2009). X-ray Polarization from Accreting Black Holes: The Thermal State. *apj*, 701:1175–1187.
- Schnittman, J. D., Krolik, J. H., and Hawley, J. F. (2006). Light Curves from an MHD Simulation of a Black Hole Accretion Disk. *apj*, 651:1031–1048.
- Stern, B. E., Begelman, M. C., Sikora, M., and Svensson, R. (1995). A large-particle Monte Carlo code for simulating non-linear high-energy processes near compact objects. *mnras*, 272:291–307.
- van der Walt, S., Colbert, S. C., and Varoquaux, G. (2011). The NumPy Array: A Structure for Efficient Numerical Computation. *Computing in Science and Engineering*, 13(2):22–30.
- Wilson, S. and Yang, Y. (2001). Chandra x-ray imaging and spectroscopy of the m87 jet and nucleus. *ApJ*, 568.
- Wong, G. N., Prather, B. S., Dhruv, V., Ryan, B. R., Mościbrodzka, M., Chan, C.-k., Joshi, A. V., Yarza, R., Ricarte, A., Shiokawa, H., Dolence, J. C., Noble, S. C., McKinney, J. C., and Gammie, C. F. (2022). PATOKA: Simulating Electromagnetic Observables of Black Hole Accretion. *ApJS*, 259(2):64.
- Xiao, F. (2006). Modelling energetic particles by a relativistic kappa-loss-cone distribution function in plasmas. *Plasma Physics and Controlled Fusion*, 48(2):203.
- Yao, Y., Zhang, S. N., Zhang, X., Feng, Y., and Robinson, C. R. (2005). Studying the Properties of Accretion Disks and Coronae in Black Hole X-Ray Binaries with Monte Carlo Simulation. *apj*, 619:446–454.
- Yuan, F., Quataert, E., and Narayan, R. (2003). Nonthermal Electrons in Radiatively Inefficient Accretion Flow Models of Sagittarius A*. *ApJ*, 598:301–312.
- Zhang, W., Dovčiak, M., and Bursa, M. (2019). Constraining the Size of the Corona with Fully Relativistic Calculations of Spectra of Extended Coronae. I. The Monte Carlo Radiative Transfer Code. *ApJ*, 875(2):148.